High-efficiency and large-numerical-aperture focusing with subdiffraction resolution using a hybrid elastic metalens

Huichun Peng and Jun Mei◉*

School of Physics, South China University of Technology, Guangzhou 510640, China

Metalenses have been widely studied and used because of their high design freedom and ultrathin configurations. For various practical applications, such as geological exploration, energy harvesting, and structural health monitoring, it is highly desirable to maximize the focusing efficiency of elastic waves. However, it is a great challenge to realize both high-efficiency focusing and subdiffraction resolution for elastic waves, especially when the mode coupling and conversion between longitudinal and transverse elastic waves is ubiquitous and inevitable. Here, we adopt a hybrid design approach for an elastic metalens to realize a high-efficiency (54.6%) and subdiffraction resolution (0.39λ) focusing performance with a large numerical aperture (NA = 0.931). The hybrid metalens is composed of a gradient metasurface in the central region and metagratings in the peripheral region to achieve a dramatic lensing functionality, where 112.5 times enhancement of wave intensity is attained at the focal spot. The high-efficiency, large-NA, and superresolution characteristics of the focusing performance, together with the planar and compact configuration of the metalens, are expected to find potential applications in various fields.

I. INTRODUCTION

Metasurfaces are two-dimensional artificial structures made of subwavelength-sized elements that are engineered to control the propagation of classical waves such as electromagnetic, acoustic, and elastic waves. Compared with three-dimensional metamaterials, metasurfaces have minimized thicknesses and planar configurations and thus are easier to manufacture and integrate with other devices. In recent years, researchers have designed various interesting metasurfaces to study and realize the focusing functionality of elastic waves, including longitudinal and transverse waves in bulk materials and Lamb and shear-horizontal modes in thin plates [1–23]. These gradient metasurfaces are based on the generalized Snell's law (GSL), and they need to accurately discretize a continuous phase shift function to implement the desired focusing functionality.

Therefore, subwavelength or even deep-subwavelength unit cells are usually utilized in the design of a metasurface-based lens, which raises challenges for high-frequency applications in terms of fabrication and integration feasibility. Furthermore, a lens with a large numerical aperture (NA) is naturally advantageous for the achievement of a high-efficiency focusing effect, which inevitably involves the contribution of wave beams with large diffraction angles. However, the diffraction efficiency of a metasurface cannot be very high at large steering angles due to the mismatched impedance between the diffracted and incident wave beams [24]. To this end, the concept of a metagrating was proposed and demonstrated [25,26]. Metagratings are based on the grating diffraction theory instead of the GSL, and they can attain almost unitary efficiency along the desired diffraction direction. Thus, the metagrating has its inherent advantage for the focusing of steep-angle wave beams. Various wave-manipulating functionalities have been successfully demonstrated with metagratings, such as anomalous reflection or refraction [27–49], nonreciprocal transmission [50,51], cloaking [52–54], far-field focusing [55–61], and other applications [62,63].

For various applications, it is highly desired to develop metalenses with large numerical apertures and high focusing efficiencies. Metasurface-based lenses have the advantage that a high refraction efficiency is easy to implement with simple unit cell configurations at small deflection angles. In contrast, it is easy for a metagrating-based lens to attain a high focusing efficiency for wave beams with large deflection angles. Combining these two configurations physically together in a collaborative way, researchers have proposed the idea of a hybrid metalens for the focusing of acoustic and electromagnetic waves [64,65]. In this way, a large-NA metalens with a high energy focusing efficiency and robust performance can be achieved, although the notion of the hyperlens has rarely been demonstrated.

On the other hand, elastic waves are associated with the mechanical vibration of particles in solid materials, such as metal, rock, and soil, and they include both

---

compressional (longitudinal) and shear (transverse) motions in the bulk material, thus are naturally more complicated than electromagnetic and acoustic waves. More importantly, the longitudinal wave (p wave) and transverse wave (s wave) components can couple with and even convert to each other when they encounter interfaces between different media. Thus, it is very challenging to focus on only one component of an elastic wave, even when the incident wave is a pure p (or s) wave, although a single-component reflected wave is highly desired in many application scenarios.

To this end, we bridge the notion of the hybrid metalens with elastic waves and, more specifically, we intelligently design the unit cells of both the metasurface and metagrating so that the mode coupling between p and s waves is almost totally suppressed. With the help of the intelligent optimization method, we design a metalens with a large NA and ultrahigh focusing efficiency for the p wave, where the field intensity at the focal spot is as high as 112.5 times the incident wave intensity. Furthermore, a superresolution focusing effect is achieved simultaneously, where the full width at half maximum (FWHM) is only 0.39λ, breaking the conventional Rayleigh-Abbe diffraction limit. The outstanding focusing performance of the proposed metalens and its underlying design paradigm may find applications in various fields such as seismic exploration, energy harvesting, and nondestructive evaluation (NDE).

With a high-numerical-aperture capability, the hybrid metalens can collect the impinging wave energy over a broader range of incident angles, which further improves the detection sensitivity of the signal in seismic exploration. For the energy harvesting application, the high intensity enhancement factor of the hybrid metalens at the focal spot provides a feasible platform with enhanced energy conversion efficiency. For the imaging and focusing applications, the hybrid metalens can provide subwavelength resolution that breaks the conventional Rayleigh-Abbe diffraction limit, which presents an alternative way to improve the performance of NDE devices. Finally, the reduced thickness of the hybrid metalens, as compared with the conventional lens where the phase change is based on the length of the ray's path inside the lens material, can substantially reduce the fabrication and assembly costs of related devices.

II. THEORETICAL ANALYSIS

To be more specific, we propose a hybrid metalens with its configuration shown in Fig. 1. The metalens is composed of two parts: a gradient metasurface (green region) in the center and two metagratings (blue region) around it. The unit cell of the metagrating contains one circular and two elliptical hollow cylinders carved in a steel substrate, with the corresponding geometrical parameters explicitly marked in Fig. 2(c). In comparison, the unit cell
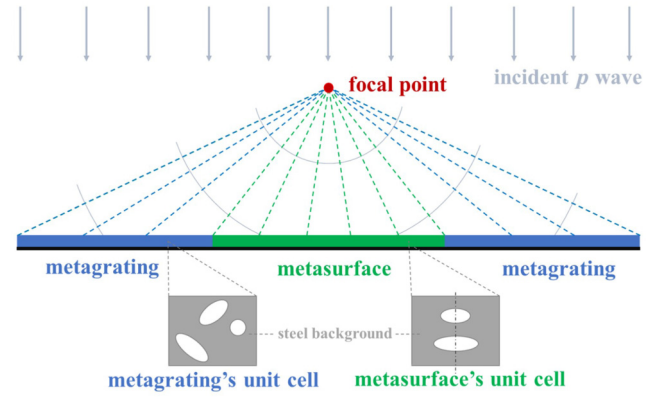

FIG. 1. Schematic diagram of the hybrid metalens, which is composed of a gradient metasurface with a metagrating on each side. For a normally incident p wave, both the metasurface and metagratings reflect the p wave towards the same focal point, with the reflected s wave totally suppressed.

of the metasurface is relatively simple, and it consists of two elliptical hollow cylinders with mirror symmetry about the y direction, as shown clearly in Fig. 2(d). Free-surface boundary conditions are applied for each cylinder's surface and at the bottom surface of the unit cell. The background material is steel, with mass density, p-wave velocity, and s-wave velocity being $\rho = 7874$ kg/m^3, $c_p = 5926$ m/s, and $c_s = 3223$ m/s, respectively. Without loss of generality, we assume that the frequency of the incident wave is $f = 200$ kHz. When a planar p wave is normally incident on the metalens, we want the reflected s wave be *totally* suppressed and the reflected p wave be *exclusively* rerouted toward a predetermined focal point.

A. Design principle of the metagrating

According to the diffraction grating theory, when a plane wave impinges on a grating with a subwavelength periodicity, it will be diffracted into several diffraction channels. For a normally incident p wave that is reflected by the metagrating, we have

$$k_p \sin \theta_p^{(m)} = m\frac{2\pi}{d}, \tag{1}$$

where k_p is the wave number of the p wave, $\theta_p^{(m)}$ is the reflection angle of the mth-order reflected p wave, and d is the periodicity of the metagrating [43]. Obviously, $\theta_p^{(0)} = 0$ represents the spectral reflection direction and cannot lead to the focusing functionality. Thus, we utilize the nonzero diffraction orders ($|m| \geq 1$) of each unit cell to realize the focusing effect.

To facilitate the design process and simplify the unit cell configuration, we utilize the first nonzero order, i.e., $|m| = 1$, to achieve the focusing effect. Taking $m = -1$st order as an example, the reflection angle $\theta_{p,L}^{(-1)}$ and periodicity d_L of
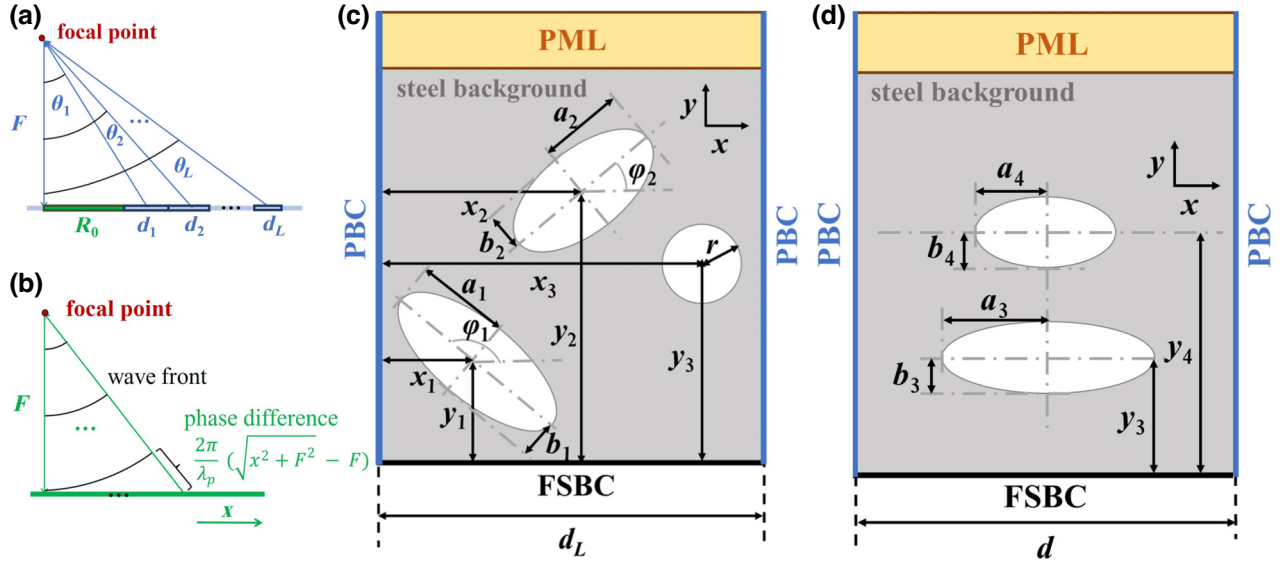
FIG. 2. (a) Design principle of the metagrating. (b) Design principle of the gradient metasurface. (c) The unit cell configuration of the metagrating, where 13 geometric parameters are explicitly marked. (d) The unit cell configuration of the metasurface, where six geometric parameters are explicitly shown. In (c),(d), periodic boundary conditions (PBCs) are applied on both sides of the unit cell, and free-surface boundary conditions (FSBCs) are applied on the bottom surface of the unit cell. A perfectly matched layer (PML) is applied on the top surface of the unit cell to absorb the reflected wave.

the Lth unit cell are related by

$$k_p \sin \theta_{p,L}^{(-1)} = -\frac{2\pi}{d_L}. \tag{2}$$

Thus, an appropriate set of $\theta_{p,L}^{(-1)}$ and d_L are needed so that each unit cell can reflect the p wave along a specific direction towards the common focal spot, as shown in Fig. 2(a). To this end, the following geometric relationship should be satisfied:

$$\tan \theta_{p,L}^{(-1)} = \frac{R_0 + \sum_{i=1}^{L} d_i - (d_L/2)}{F}, \tag{3}$$

where R_0 is the distance from the first unit cell of the metagrating to the axis of the hybrid metalens (R_0 is also the half width of the metasurface), and F represents the focal length. To achieve a far-field focusing effect, we let $F = 20\lambda_p$, where $\lambda_p = 29.63$ mm is the wavelength of the p wave at 200 kHz. Accordingly, the reflection angle of the first unit cell is set as $\theta_{p,1}^{(-1)} = 39°$. Thus, we have $R_0 = 15.4\lambda_p$, and the total width of the metasurface is $30.8\lambda_p$. With Eqs. (2) and (3), the values of $\theta_{p,L}^{(-1)}$ and d_L for each unit cell can be uniquely determined. In this way, the p waves diffracted by all unit cells converge to the same focal spot, leading to the desired focusing functionality. The metagrating consists of 30 unit cells on each side of the lens, covering an angular range of $39° \le |\theta_p| \le 68.57°$.

We note that, due to the mode coupling and mutual conversion between p and s waves, even when the incident wave is a pure p wave, the reflected wave usually contains both p and s waves. For a normally incident p wave, the direction of the reflected s wave is given by

$$k_s \sin \theta_{s,L}^{(n)} = n\frac{2\pi}{d_L}, \tag{4}$$

where k_s is wave number of the s wave, $\theta_{s,L}^{(n)}$ is the reflection angle of the nth order s wave reflected by the Lth unit cell. Thus, for $\theta_{p,1}^{(-1)} \ge 39°$, there exist only five propagation channels ($|n| = 0, 1, 2$) for the reflected s wave. Otherwise, more diffraction channels of the s wave need to be controlled.

In this work, we aim to achieve a high-efficiency focusing effect for the p wave and, therefore, we need to greatly or even totally suppress the s-wave component in the reflected wave. To be more specific, for each unit cell of the metagrating we need to reroute the p wave *exclusively* along only one single diffraction channel (e.g., the $m = -1$ channel) among all three channels of the p wave, and at the same time we need to eliminate all five channels of the s wave. Obviously, it is nontrivial to simultaneously manipulate eight diffraction channels for each unit cell. For this purpose, we utilize the genetic algorithm (GA) as an intelligent optimization algorithm to fulfill the design task.

The unit cell configuration of the metagrating is illustrated in Fig. 2(c), which has 13 geometrical parameters, including the semimajor axes a_1 and a_2, semiminor axes b_1 and b_2, rotation angles φ_1 and φ_2, center positions of the two elliptical cylinders (x_1, y_1) and (x_2, y_2), as well as the

TABLE I. Optimized geometrical parameters of unit cells of the metagratings.

| Group index	L	d_L (mm)	$\|\theta_{p,L}^{(-1)}\|$ (deg)	a_1 (mm)	b_1 (mm)	φ_1 (deg)	x_1 (mm)	y_1	a_2 (mm)	b_2 (mm)	φ_2 (deg)	x_2 (mm)	y_2 (mm)	r (mm)	x_3 (mm)	y_3 (mm)
1	1	47.08	39.00	10.7630	4.8301	−54.0610	24.3911	38.3957	4.1494	1.7895	40.1314	9.7295	38.4878	3.2060	11.0931	8.8681
2	2	44.65	41.58	11.4014	5.2165	−53.9778	24.9606	39.1523	4.4629	1.9811	37.7906	11.0459	40.5467	4.2578	8.8710	7.3900
3	3	42.76	43.86	8.6303	4.6989	−57.2040	16.4936	40.4903	2.5150	1.6615	−40.3233	8.6297	41.3488	2.5034	8.3834	8.0396
4	4	41.26	45.90	9.4926	4.0896	−57.5640	15.9179	40.9055	2.3895	1.6272	−45.8102	8.1524	42.5382	2.4780	7.7464	7.4168
5	5	40.04	47.74	9.1958	3.6502	−56.9111	15.5748	40.7083	2.3226	0.9258	−50.2971	7.6129	43.2957	2.5132	7.6859	6.7949
6	6	39.02	49.41	9.1807	3.3898	−58.1459	15.9017	40.7479	2.3288	0.7653	−50.6423	7.8549	43.5239	2.5648	7.7329	6.6002
7	7	38.16	50.94	9.0338	2.7746	−60.2270	15.8823	40.5658	2.2936	1.0054	−56.5528	6.1985	43.6569	2.2458	7.6634	5.8424
8	8	37.42	52.35	9.3043	2.5468	−57.7653	16.7547	40.3991	2.6716	1.6465	−48.5845	6.5245	43.8597	2.2638	7.8192	6.3286
9	9	36.79	53.65	10.7946	2.6601	−53.5771	16.7383	40.0382	2.7267	2.4654	−86.1546	5.8614	43.9455	1.8127	7.4945	6.8935
10	10	36.24	54.85	10.4906	2.7274	−53.0607	16.9828	40.6784	2.9788	2.4650	−85.2349	6.0448	45.2102	2.1914	8.5115	7.5302
11	11	35.75	55.97	10.4262	2.4952	−54.0588	17.1898	41.0175	3.1915	2.2614	−57.3616	6.6020	45.6916	2.8391	8.9821	7.3703
12	12	35.32	57.02	10.4031	2.4412	−54.2039	18.0376	41.1881	3.3953	2.0802	−56.3128	7.6295	46.4495	2.9328	9.8533	7.7371
13	13–15	34.94, 34.60, 34.29	58.00, 58.92, 59.78	10.2565	2.4474	−55.8629	19.4847	41.0180	4.0557	2.0412	−44.8482	8.7274	47.1246	3.1040	9.7292	7.5923
14	16–20	34.01, 33.76, 33.53, 33.32, 33.12	60.60, 61.37, 62.10, 62.79, 63.45	9.1489	2.0835	−51.3847	20.9375	41.1775	5.3824	2.1262	−43.1858	8.7393	47.3824	3.7520	7.0255	5.5232
15	21–25	32.95, 32.78, 32.63, 32.49, 32.36	64.07, 64.67, 65.23, 65.77, 66.29	9.3423	2.2876	−56.7111	20.0932	41.1225	5.4263	2.2741	−54.7041	8.7853	48.4510	3.3944	8.6360	5.8323
16	26–30	32.24, 32.13, 32.02, 31.92, 31.83	66.79, 67.26, 67.72, 68.15, 68.57	9.6068	2.3302	−53.5677	19.1916	40.9068	6.0545	1.6395	−63.8568	9.4195	48.0909	4.6099	9.5551	6.3512
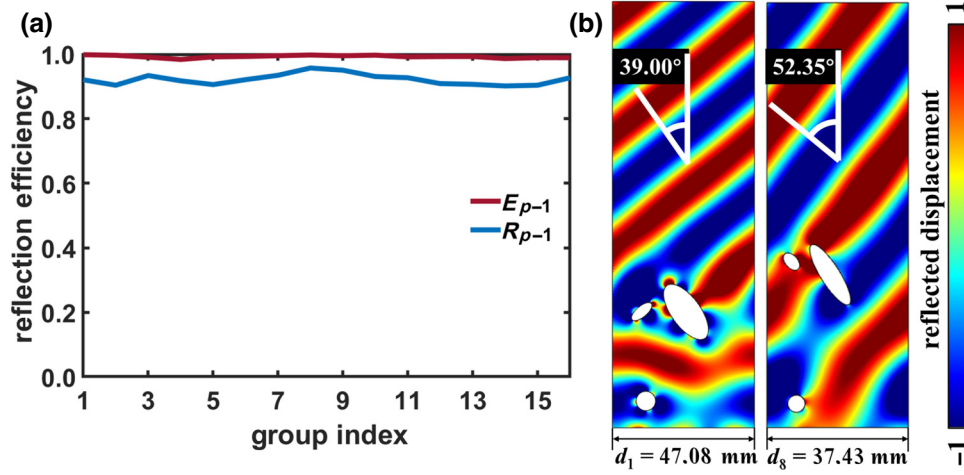
FIG. 3.   Reflection efficiency of the metagrating. (a) Reflection efficiency of all unit cells along the p_{-1} channel. $E_{p_{-1}}$ denotes the ratio of energy along p_{-1} channel to the energy of all p channels. $R_{p_{-1}}$ represents the ratio of energy along p_{-1} channel to the total energy. (b) Reflected p-wave displacement fields for the first and eighth unit cells, respectively, where the reflection angles $\theta_1 = 39.0°$ and $\theta_8 = 52.35°$.

radius r and center position (x_3, y_3) of the circular cylinder. These 13 structural parameters of each unit cell are simultaneously and intelligently optimized with the GA to steer the reflected p wave exclusively along the -1st diffraction channel, as shown in Fig. 2(a).

B. Design principle of the metasurface

In contrast, a metasurface is designed according to the GSL instead of grating diffraction theory. To this end, the subwavelength unit cells of the metasurface are specifically designed to precisely control the phase shift at the

desired focal spot. A focusing effect can be achieved with a metasurface if the following phase profile can be realized:

$$\Phi(x) = \frac{2\pi}{\lambda_p}\left(\sqrt{x^2 + F^2} - F\right), \tag{5}$$

where Φ is the required phase shift when the p wave is reflected by the unit cell at position x, λ_p is the wavelength of the p wave, and F is the focal length [65]. This design principle is schematically shown in Fig. 2(b). In Eq. (5) the phase shift Φ is a continuous function of the transverse
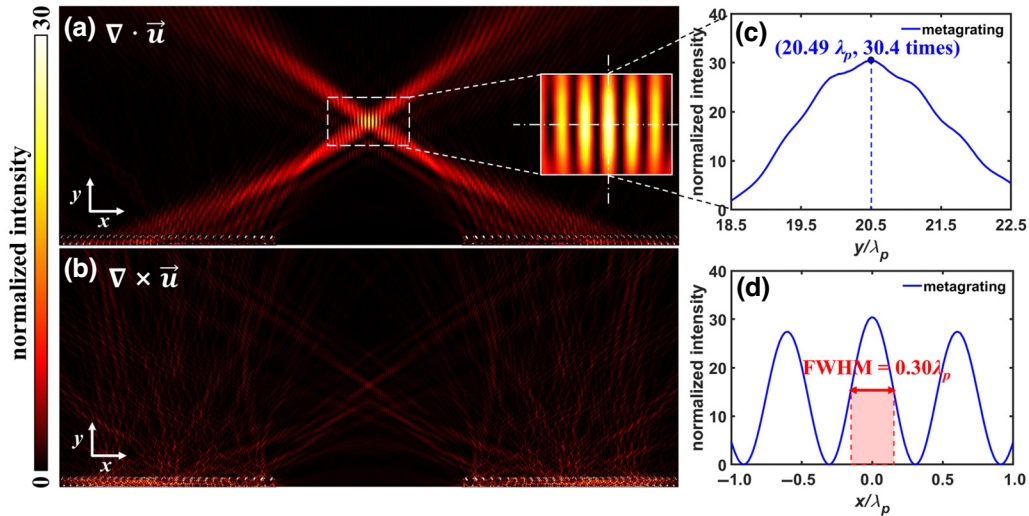

FIG. 4.   Focusing performance of the metagrating-based lens. (a) Normalized displacement field intensity of the reflected p wave, where the inset shows the enlarged view around the focal point. (b) Normalized displacement field intensity of the reflected s wave. (c) Normalized intensity profile along the axis of the lens, where the maximum value 30.4 is reached at $y = 20.49\lambda_p$. (d) Normalized intensity profile along the x direction at the focal spot, where the FWHM is $0.30\lambda_p$.
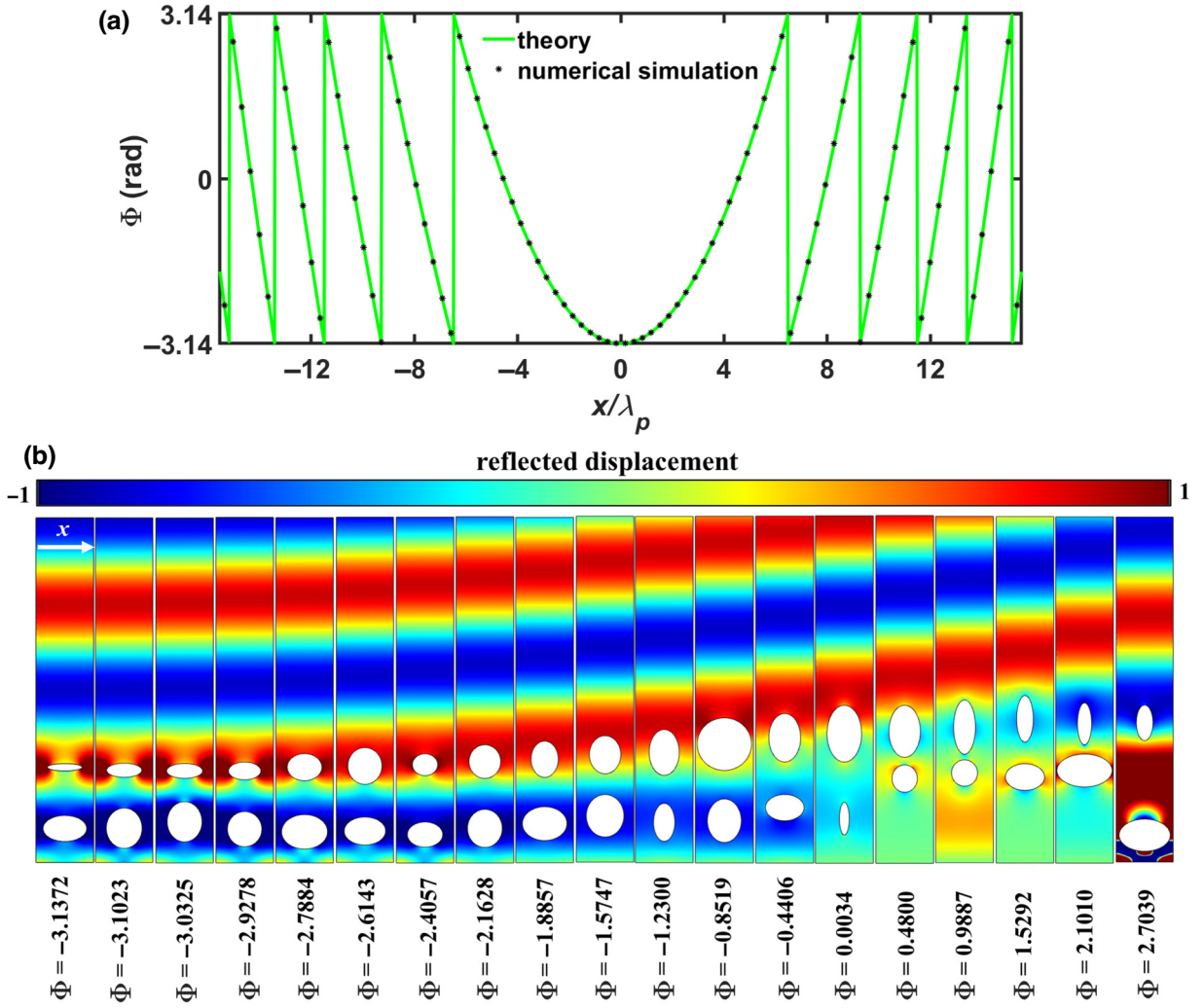
FIG. 5. The design of the metasurface. (a) The phase profile Φ of the metasurface for a 200-kHz incident p wave with a focal length $F = 20.49\lambda_p$. (b) Normalized displacement amplitude for the first 19 unit cells of the metasurface, where a phase shift of 2π is covered.

position x, and for a practical design it is approximated by discrete unit cells of the metasurface.

Figure 2(d) shows the unit cell configuration of the metasurface, where two elliptical hollow cylinders with heights y_3 and y_4, respectively, are positioned at the center of the unit cell, with their semimajor axes a_3 and a_4 (semiminor axes b_3 and b_4) parallel to the x direction (y direction). Thus, there are six parameters that need to be optimized to achieve the desired phase shift Φ.

As mentioned previously, the gradient metasurface has a total width of $30.8\lambda_p$. Now we discretize the desired phase shift $\Phi(x)$, i.e., Eq. (5), with 92 unit cells, where a typical unit cell has a subwavelength periodicity of 10 mm (e.g., $0.3375\lambda_p$). After taking the mirror symmetry into consideration, we only have to optimize the configurations of 46 unit cells. Here we utilize the GA to find the structural parameters of each unit cell.

C. Hybrid metalens

At this stage we integrate the gradient metasurface with two metagratings to form a hybrid metalens. The metasurface is designed to reflect and focus the p wave incident on the central region of the lens, covering a reflective angle range of $0° \leq |\theta_p| \leq 39°$. The metagratings are designed to reflect and focus the p wave incident on the peripheral region of the lens, responsible for a reflective angle range of $39° \leq |\theta_p| \leq 68.57°$. The hybrid metalens, with a high $\mathrm{NA} = \sin(68.57°) = 0.931$, can achieve a wide-angle high-efficiency focusing effect, as demonstrated in the subsequent section.

III. RESULTS AND DISCUSSIONS

In this section, we demonstrate the focusing effect of the metagrating-based lens, metasurface-based lens, and hybrid metalens, respectively.

TABLE II. Optimized structural parameters of unit cells of the metasurface.

Unit cell no.	a_3 (mm)	b_3 (mm)	y_3 (mm)	a_4 (mm)	b_4 (mm)	y_4 (mm)
1	3.7894	2.2715	5.9047	3.0277	0.6416	16.5661
2	3.1109	3.5063	5.9421	3.0563	1.2336	16.0440
3	3.0199	3.4994	7.1424	3.1142	1.2984	15.9958
4	2.9833	3.0506	5.8500	2.8082	1.5504	15.9591
5	3.9838	2.9924	5.3890	3.0017	2.3580	16.6250
6	3.6126	2.4297	5.4279	2.9759	3.1992	16.7351
7	3.0679	2.1792	4.9164	2.1915	1.8995	17.0406
8	3.0007	3.2953	5.9865	2.7366	2.9123	17.5561
9	3.8485	2.9384	6.7847	2.3514	3.1489	17.9738
10	3.2543	3.6855	8.0242	2.7204	3.2970	18.6121
11	1.8399	3.2907	6.9904	2.5976	3.9708	19.1065
12	2.9120	3.7685	7.2927	4.6746	4.5520	20.5446
13	3.3264	2.2745	9.5877	2.7386	4.1883	21.6624
14	0.8496	2.8187	7.6969	2.9851	4.8986	22.3673
15	2.1986	2.3632	14.6184	2.7222	4.4991	22.7684
16	2.2462	2.2842	15.5393	1.8876	4.6953	23.4935
17	3.3938	2.3147	14.8846	1.4410	4.0334	24.9738
18	4.7736	2.8523	16.0409	1.2225	3.6286	24.1289
19	4.4708	2.8009	4.6631	1.4524	3.0918	24.1939
20	3.6973	2.9848	5.8624	3.0470	1.8084	16.3335
21	2.9717	2.8432	6.1679	3.2717	2.8106	17.7125
22	3.0189	3.2624	7.7963	2.5499	2.7720	18.6751
23	2.9247	1.4107	7.4464	4.6949	4.5164	20.5439
24	3.3260	2.3043	9.5490	0.7365	4.0321	21.7566
25	3.2848	2.2215	15.0069	2.6138	4.5170	22.8454
26	2.5016	2.2171	16.1084	1.1246	4.0491	24.8019
27	4.7156	3.3228	16.1534	1.6163	3.1318	23.0638
28	3.6219	3.4746	6.9942	3.7073	1.8887	16.2697
29	3.1223	1.5335	7.1310	3.7651	2.7625	18.1392
30	1.3485	3.2845	5.5627	2.5983	2.4747	19.1071
31	3.3957	2.3472	10.4728	2.7621	4.6154	21.4559
32	4.8064	3.7303	14.6278	2.5417	2.2626	21.9397
33	3.4981	2.4860	14.8087	1.1536	3.4598	24.7779
34	3.9292	3.8185	5.2005	2.9133	2.4089	24.3566
35	3.8562	2.3281	5.4996	3.5768	3.7834	16.6542
36	3.2643	3.6085	7.7265	2.8819	3.8576	18.5882
37	1.2786	1.8046	8.6352	3.0050	3.8280	21.3168
38	4.7608	3.7347	14.6543	2.5426	2.2883	22.1351
39	3.2624	2.4194	15.5350	0.8701	3.1699	24.4094
40	4.4507	1.1318	16.7706	1.0092	3.6665	23.7581
41	3.3500	2.4215	7.0731	3.6907	3.0626	17.8579
42	2.6211	3.7527	7.2269	3.4398	3.5600	20.5089
43	1.2352	2.9937	8.7322	3.4684	4.7802	22.8115
44	2.8712	2.9700	14.6424	1.5643	4.0586	24.6252
45	4.4497	1.1214	16.6971	1.4211	3.6237	23.6569
46	3.0794	2.3913	4.3450	1.3891	1.5527	17.3369

A. Metagrating-based lens

For the metagrating region of the lens, the smallest reflection angle is 39°, where each unit cell can reflect the incident wave along three p-wave channels (p_{-1}, p_0, p_1) and five s-wave channels ($s_{-2}, s_{-1}, s_0, s_1, s_2$). Taking the right half of the metalens as an example, we need to substantially suppress or even eliminate the wave energy along seven channels ($p_0, p_1, s_{-2}, s_{-1}, s_0, s_1, s_2$) so that the reflected energy propagates along the p_{-1} channel *exclusively*. To this end, we set the following two optimization objectives when applying the GA: One is $R_{p_{-1}}$, the ratio of the wave energy along the p_{-1} channel to the total wave energy. The other is $E_{p_{-1}}$, the ratio of the wave energy along the p_{-1} channel to the wave energy along all p-wave channels. By optimizing $R_{p_{-1}}$ and $E_{p_{-1}}$ simultaneously, we can achieve the desired focusing effect that all reflected
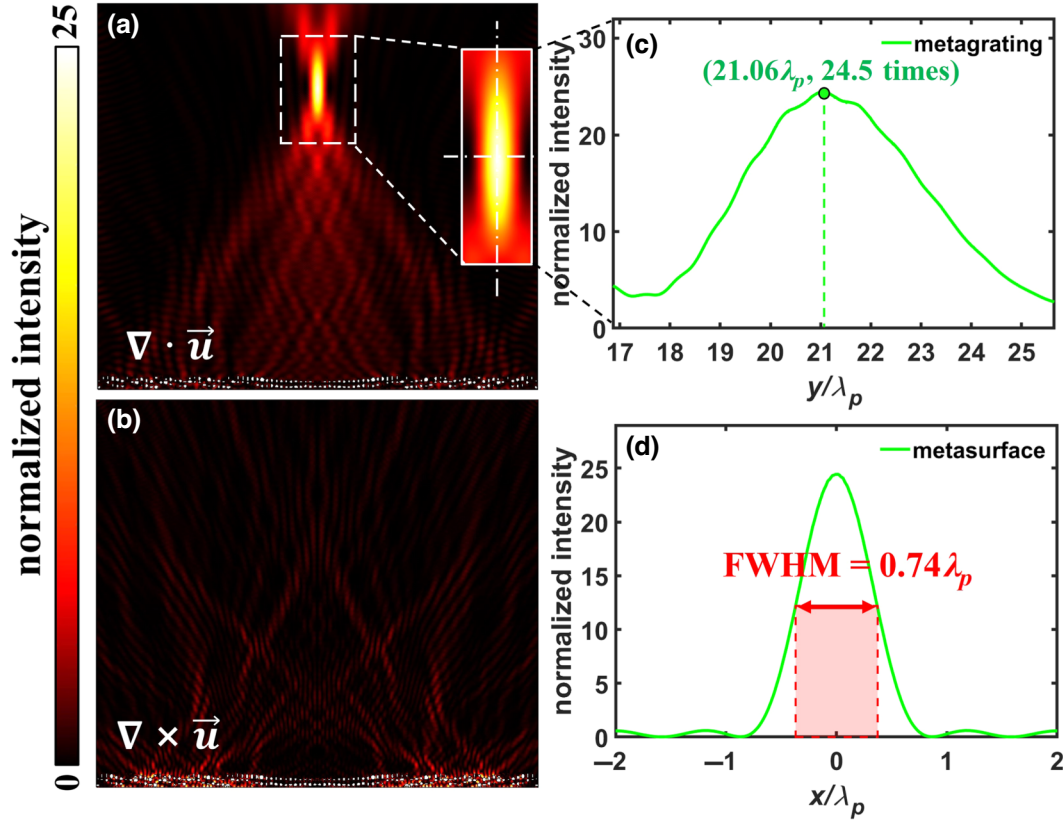
FIG. 6. Focusing performance of the metasurface-based lens. (a) Normalized displacement field intensity of the reflected p wave, where the inset shows the enlarged view around the focal point. (b) Normalized displacement field intensity of the reflected s wave. (c) Normalized intensity profile along the axis of the lens, where the maximum value 24.5 is reached at $y = 21.06\lambda_p$. (d) Normalized intensity profile along the x direction at the focal spot, where the FWHM is $0.74\lambda_p$.

s-wave channels are greatly suppressed, and at the same time all reflected p waves are directed along the p_{-1} channel exclusively.

On each side of the lens, the metagrating is composed of 30 unit cells, and we need to optimize the geometrical parameters of all unit cells. Since the unit cell's structure does not change much when the diffraction angle is large enough, we find that neighboring unit cells can share the same set of geometrical parameters. In this way, only 16 independent sets of parameters are needed to construct the 30 unit cells, which greatly simplifies the design process. The detailed configurations of all unit cells are listed in Table I, where we can see that only 16 groups of parameters are needed. For example, the 13th, 14th, and 15th unit cells share the same set of parameters, which is the 13th group of parameters, corresponding to group index 13 in the table.

The reflection efficiency for each group of geometrical parameters is plotted in Fig. 3(a), where we observe that $E_{p_{-1}} > 98\%$ and $R_{p_{-1}} > 90\%$ for all groups, which means that the wave energy along the p_{-1} channel represents an overwhelming proportion of the total energy, which is exactly what we desire. This is a surprising result because

it is well known that, due to mode coupling and conversion, even when the incident wave is a pure p wave, the reflected wave usually contains both p and s waves. With the help of the GA-based intelligent design, here we successfully suppress the reflection of s waves and at the same time redirect the p wave along the p_{-1} channel exclusively. Figure 3(b) verifies the desired wave manipulating effect. The p wave displacement fields reflected by the first and eighth unit cells unambiguously exhibit the planar wave front of the p wave along the desired p_{-1} channel with high efficiency.

We then assemble the 30 unit cells into a metagrating on both sides of the metalens, and the resultant focusing effect is shown in Fig. 4. We use $\vec{u}_p$ and $\vec{u}_s$ to represents the p- and s-wave components of the total displacement vector $\vec{u}$, respectively, and it follows that $\left|\vec{u}_p\right| = \left|\vec{\nabla} \times \vec{u}/ik_p\right|$ and $\left|\vec{u}_s\right| = \left|\vec{\nabla} \times \vec{u}/ik_s\right|$. In this way, Figs. 4(a) and 4(b) show the normalized displacement field intensity of reflected p and s waves with the same color scale, respectively, where the intensity is normalized to the incident p wave.
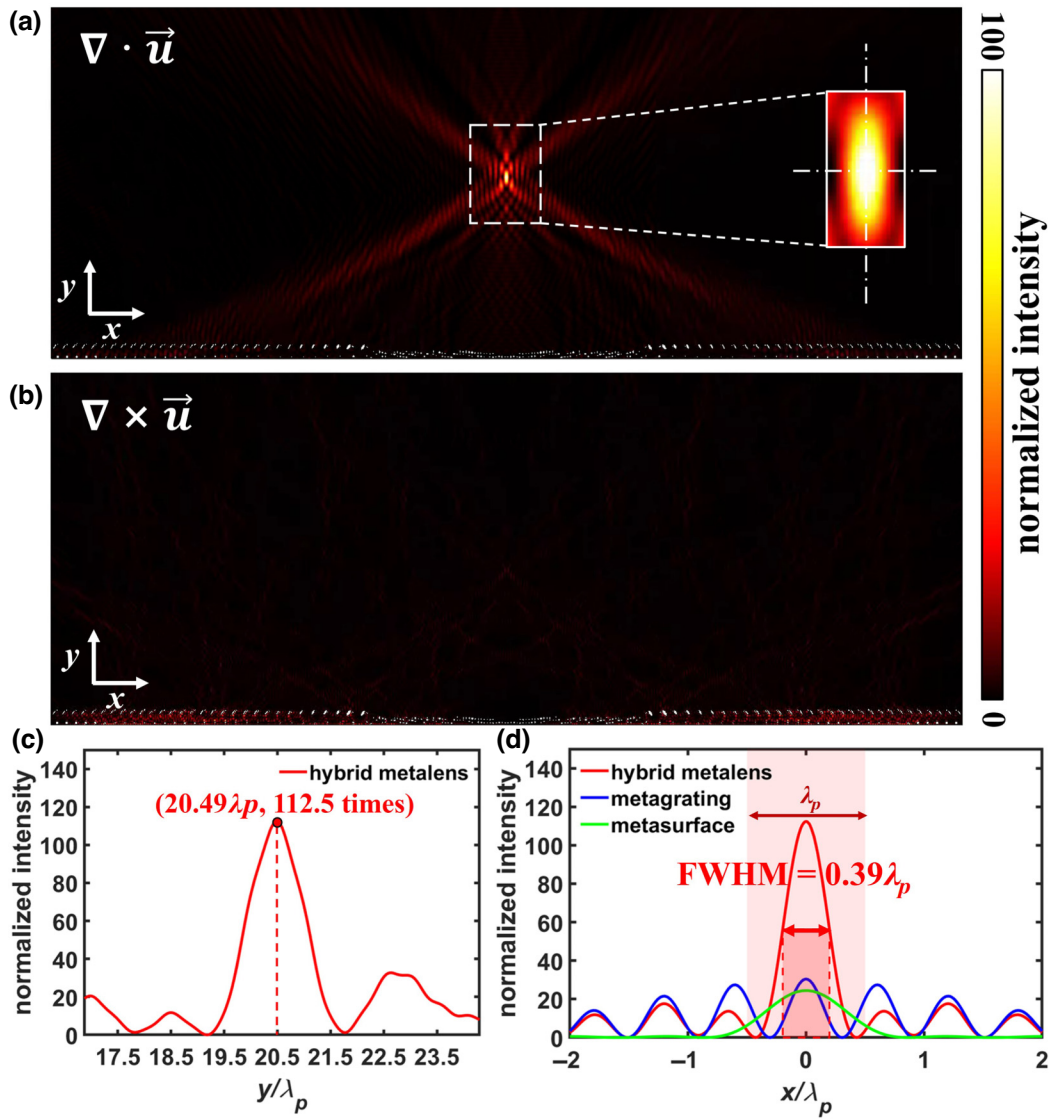
FIG. 7. Focusing performance of the hybrid metalens. (a) Normalized displacement field intensity of the reflected p wave, where the inset shows the enlarged view around the focal point. (b) Normalized displacement field intensity of the reflected s wave. (c) Normalized intensity profile along the axis of the lens, where the maximum value 112.5 is reached at $y = 20.49\lambda_p$. (d) Normalized intensity profile along the x direction at the focal spot, where the FWHM is $0.39\lambda_p$.

Obviously, the reflected s wave is greatly suppressed, as shown in Fig. 4(b). A small focusing region containing several bright stripes is obtained for the reflected p wave, as shown in the enlarged view in Fig. 4(a). The normalized intensity profile along the axis of the lens is plotted in Fig. 4(c), where the maximum value of 30.4 is reached at $y = 20.49\lambda_p$. Thus, a high-efficiency focusing effect is achieved around the focal spot, with an intensity enhancement of 30.4 times in terms of the incident wave intensity.

The initial design target of the focal length is $F = 20\lambda_p$. One reason behind the small difference between the numerical result ($20.49\lambda_p$) and the theoretical value of focal length could be that the practical configuration

of each unit cell has a nonzero and finite thickness. However, the thickness of each unit cell is neglected in the design paradigm, as shown schematically in Fig. 2(a). Thus, it is not strange that the actual position of the focal spot is a little bit higher than $20\lambda_p$, which is consistent with the full-wave numerical simulations.

The normalized intensity profile along the transverse direction (i.e., along the x direction) at the focal spot is plotted in Fig. 4(d), where the FWHM is found to be $0.30\lambda_p$, implying a high-resolution focusing.

In the literature, the focusing efficiency is defined as the ratio of the power in the focal plane with a radius of 3 times the FWHM to the total power of the incident light [65]. For

the metagrating-based lens, we find the focusing efficiency is 35.8%.

B. Design of metasurface-based lens

For the metagrating-based lens, the actual focal spot is located at $F = 20.49\lambda_p$. With this focal length, we can obtain the required phase shift of the metasurface, i.e., $\Phi(x) = 2\pi/\lambda_p \left(\sqrt{x^2 + F^2} - F \right)$, which is plotted as a green line in Fig. 5(a). Then we use 46 unit cells to discretize this continuous phase function, which are marked by black dots in Fig. 5(a). Based on the GA, the optimized geometrical parameters of the unit cells are listed in Table II. For example, the implementation of the first 19 unit cells covers a phase shift range of 2π, as shown in Fig. 5(b).

We assemble these 46 unit cells into a metasurface-based lens, whose focusing effect is shown in Fig. 6. Figures 6(a) and 6(b) show the normalized displacement intensity of the reflected p and s waves, respectively, with the same color scale. For the p wave, a very bright focal spot can be identified, and an enlarged view of the wave intensity is provided in the inset. In comparison, the intensity of the reflected s wave is much weaker.

The normalized intensity profile along the lens's axis is plotted as a green line in Fig. 6(c), where a maximum value of 24.5 is attained at $y = 21.06\lambda_p$, implying a significant enhancement of the wave intensity at the focal spot. In comparison with the metagrating-based lens, here the position of the focal spot is shifted upward slightly. Since the bright spot has an elliptic shape with its semimajor axis along the y direction, its overlap with the metagrating's focusing pattern is expected to further increase the maximum wave intensity.

The normalized intensity profile along the x direction at the focal spot is plotted in Fig. 6(d), where the FWHM is found to be $0.74\lambda_p$. The focusing efficiency of the metasurface-based lens is found to be 63.2%.

C. The hybrid metalens

Finally, we combine the metagratings with the gradient metasurface to construct a hybrid lens, with the resultant focusing effect shown in Fig. 7. Figures 7(a) and 7(b) illustrate the normalized intensity of the reflected p and s waves, respectively. Obviously, the p wave is highly concentrated around the focal point, as shown in the enlarged view. With the same color scale, the intensity of the s wave is almost negligible, as clearly shown in Fig. 7(b).

The normalized intensity profile along the lens's axis is plotted in Fig. 7(c), where the maximum value of 112.5 is achieved at $y = 20.49\lambda_p$. It is exciting to obtain such a high enhancement factor (112.5) in terms of the incident wave intensity, which is significantly larger than that of a metasurface-based lens (24.5) and a metagrating-based lens (30.4). This ultrahigh-efficiency focusing effect is achieved through a compact and planar lens with a wavelength thickness, and is expected to find potential applications in various fields, such as geological exploration and energy harvesting.

In Fig. 7(d) we plot the normalized intensity profiles along the x direction at the focal spots for the metagrating-based lens, metasurface-based lens, and hybrid lens, respectively. It is well known that the conventional Rayleigh-Abbe diffraction limit is $0.5\lambda_p/\text{NA} = 0.537\lambda_p$ [66,67]. The FWHM of the hybrid metalens is $0.39\lambda_p$, which is lower than $0.5\lambda_p/\text{NA}$ and implies a superresolution focusing effect that breaks the Rayleigh-Abbe limit. In addition, the focusing efficiency of the hybrid lens is also very high and found to be 54.6%.

In reality, there is always a loss for a material. We have conducted a study of the focusing effect influenced by the material loss, and the detailed discussion can be found in Appendix A.

In Appendix B we have also constructed a metasurface-based lens that has the same length as the hybrid metalens, and compare these two metalenses in terms of their focusing performances.

IV. CONCLUSION

We propose a hybrid metalens consisting of a gradient metasurface surrounded by metagratings on both sides. This hybrid metalens inherits the merits of both the metagrating and metasurface and has a large NA and an ultrahigh focusing efficiency. With the intelligent design of each unit cell and the intentional suppression of mode coupling and conversion between the p and s waves, the metalens exhibits an extraordinarily high focusing performance for a normally incident p wave. In particular, the intensity enhancement factor around the focus is found to be 112.5 in terms of the incident wave intensity, implying a huge energy concentration effect of the hybrid metalens. In addition, the transverse FWHM in the focal plane is only $0.39\lambda_p$, breaking the conventional Rayleigh-Abbe diffraction limit. The high-efficiency (54.6%), large-NA (0.931), and superresolution ($0.39\lambda_p$) of the focusing performance, together with the planar and compact configuration of the metalens, is expected to find potential applications in various fields such as geological exploration, seismic wave signal sensing, and nondestructive structure detection.

APPENDIX A: THE INFLUENCE OF MATERIAL LOSS ON THE FOCUSING EFFECT

In this appendix, we have conducted a study of the focusing effect influenced by the material loss. In particular, we consider the Young's modulus $E = 211(1 + \eta i)$ GPa and Poisson's ratio $\nu = 0.29$ for the steel background, with $\eta = 0.001$ denoting the material loss. In this way, we have $c_p = (5926 + 2.96i)$ m/s and $c_s = $
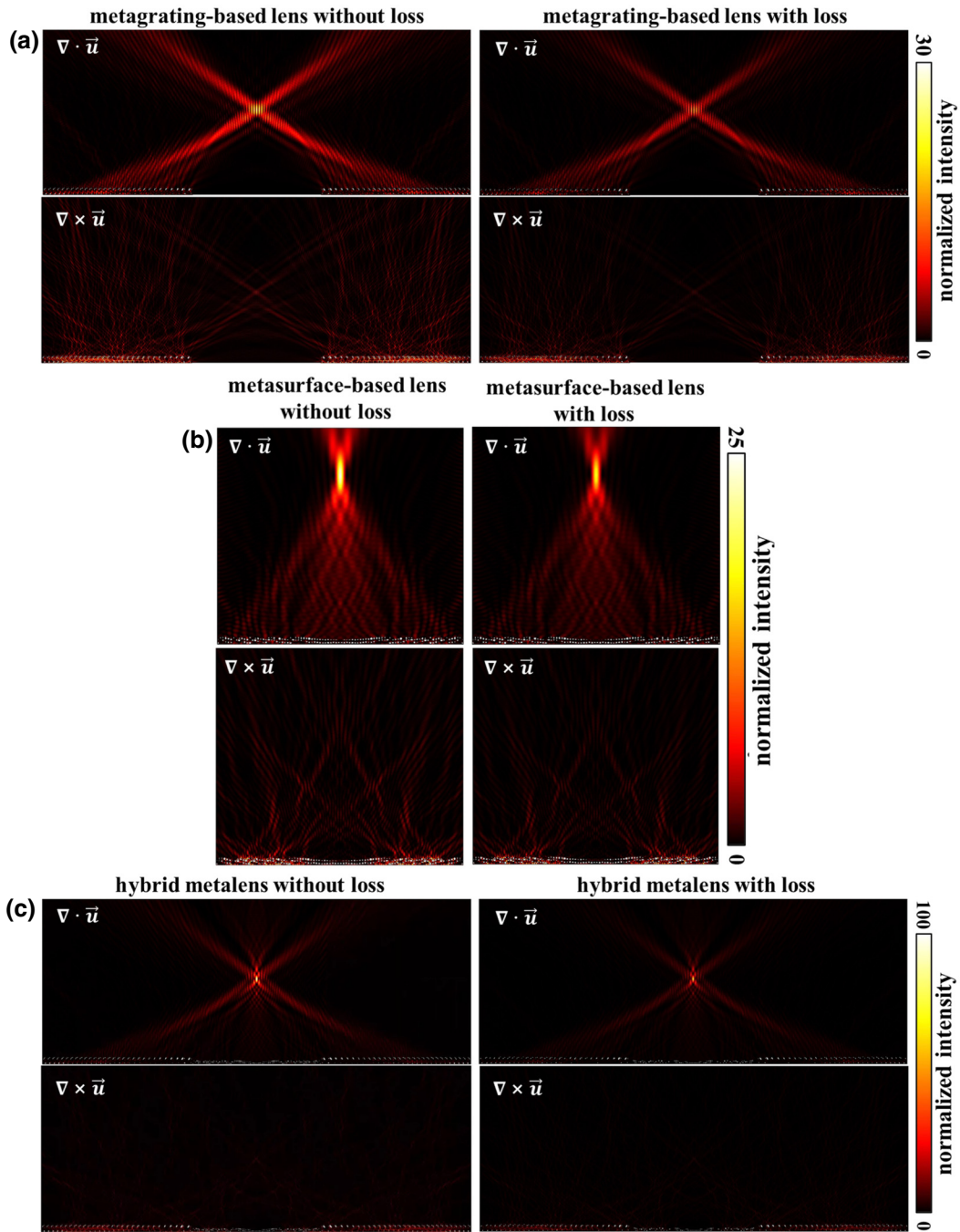
FIG. 8. The influence of material loss on the focusing effect. (a)–(c) The focusing effects without and with material loss for the metagrating-based lens, metasurface-based lens, and hybrid metalens, respectively.

$(3223 + 1.61i)$ m/s. The corresponding focusing effects are demonstrated in Fig. 8. We can see that the s-wave component is further suppressed, and at the same time the p-wave focusing effect is reserved to a large extent.

APPENDIX B: COMPARISON OF METALENSES WITH THE SAME LENGTH

In the current design of the metagrating-based lens, the reflective angle of the first unit cell is set as $\theta_{p,1}^{(-1)} = 39°$.

The reason is that, according to the grating diffraction theory, we have $k_p \sin \theta_{p,L}^{(m)} = m(2\pi/d_L)$ and $k_s \sin \theta_{s,L}^{(n)} = n(2\pi/d_L)$, where $k_{p(s)}$ is the wave number of the p (s) wave, and $\theta_{p,L}^{(m)}$ and $\theta_{s,L}^{(n)}$ are the reflective angle of the mth-order p wave and the nth-order s wave reflected by the Lth unit cell, respectively. Thus, if we have $\theta_{p,L}^{(-1)} \geq 39°$ for *all* unit cells of the metagrating, there will be only five propagation channels ($|n| = 0, 1, 2$) for the reflected
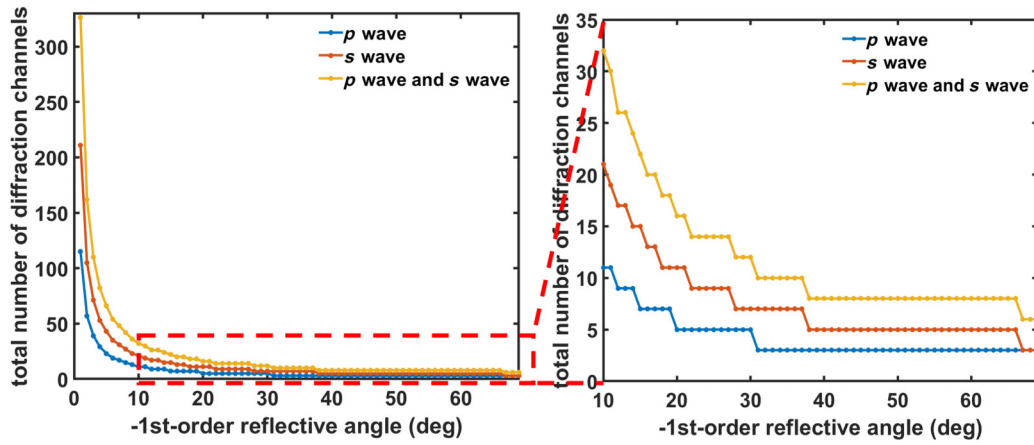
FIG. 9.   Relationship between the total number of diffraction channels and reflective angle.

s wave, and three propagation channels ($|n| = 0$, 1) for the reflected *p* wave. To fulfill the focusing functionality, we need to simultaneously control up to eight diffraction channels so that the reflected wave energy is redirected *exclusively* along the p_{-1} channel. For this purpose, each unit cell has to contain at least three hollow cylinders to

provide enough degrees of freedom for the optimization algorithm.

Instead, if the reflective angle $\theta_{p,L}^{(-1)}$ is smaller than $39°$, we have to simultaneously manipulate *more* diffraction channels. To be more specific, in Fig. 9 we plot the total number of diffraction channels as a function of the
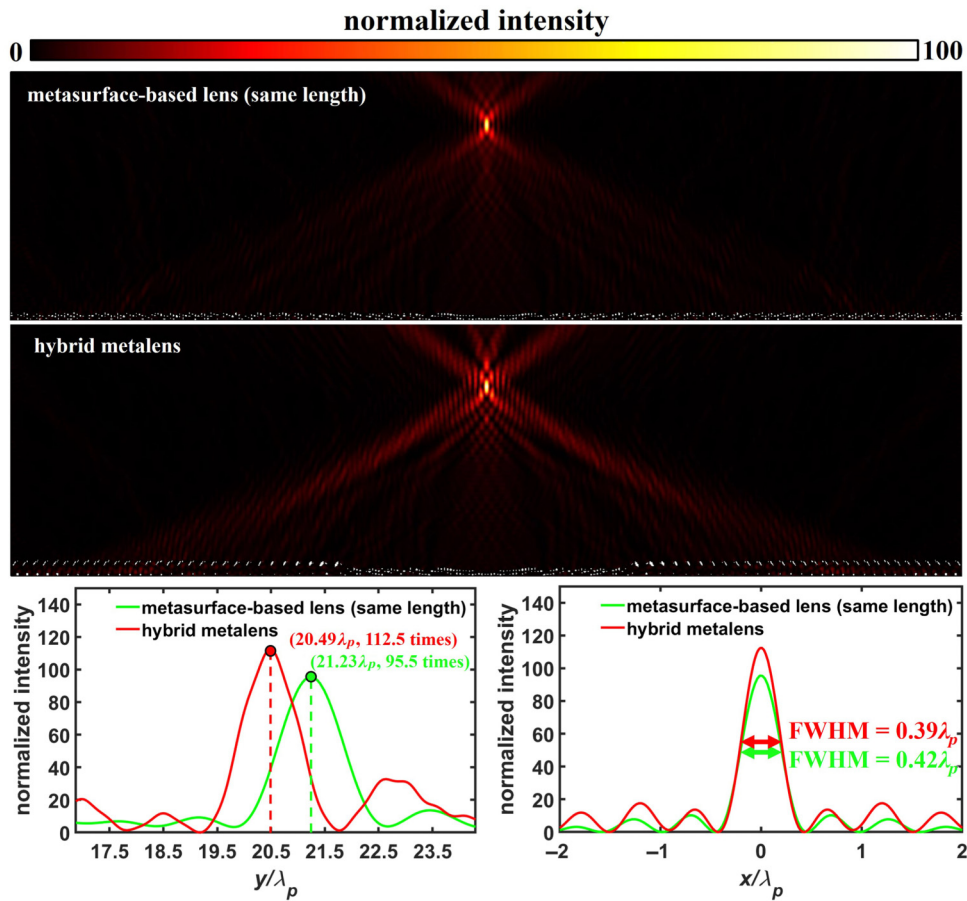

FIG. 10.   The focusing effect comparison of a metasurface-based lens and a hybrid lens with the same length.

TABLE III. Comparison between a metasurface-lens and a hybrid metalens with the same length.

	Metasurface-based lens	Hybrid metalens
Wave intensity enhancement factor	95.5	112.5
Focusing efficiency (%)	46.6	54.6
FWHM (λ_p)	0.42	0.39

reflection angle. As shown explicitly in the figure, when $\theta_{p,L}^{(-1)} = 15°$, we need to simultaneously control as many as 22 diffraction channels (7 p-wave channels + 15 s-wave channels) for this meta-atom to realize the required functionality. This will pose a huge challenge and eventually an impossible optimization task for the meta-atom's design. It is for this reason that the metagrating-based lens covers a reflective angle range of $39° \leq |\theta_p| \leq 68.57°$ in the current design.

In contrast, there is no limitation on the metasurface-based lens, i.e., the diffraction angle of the metasurface can cover the whole range of $0° \leq |\theta_p| \leq 68.57°$. Thus, we can design a metasurface-based lens with the same length as the hybrid metalens.

To this end, we use 153 unit cells to discretize the phase function $\Phi(x) = 2\pi/\lambda_p \left(\sqrt{x^2 + F^2} - F \right)$, and construct a metasurface-based lens with the same length as the hybrid metalens. The focusing effects of these two metalenses are shown in Fig. 10, and the corresponding characteristics are summarized in Table III. Both the figure and the table explicitly show that the hybrid metalens exhibits a more satisfactory focusing performance.

---

[1] Y. Liu, Z. Liang, F. Liu, O. Diba, A. Lamb, and J. Li, Source illusion devices for flexural Lamb waves using elastic metasurfaces, Phys. Rev. Lett. **119**, 034301 (2017).

[2] H. Nassar, B. Yousefzadeh, R. Fleury, M. Ruzzene, A. Alù, C. Daraio, A. N. Norris, G. Huang, and M. R. Haberman, Nonreciprocity in acoustic and elastic materials, Nat. Rev. Mater. **5**, 667 (2020).

[3] R. Zhu, X. N. Liu, G. K. Hu, C. T. Sun, and G. L. Huang, Negative refraction of elastic waves at the deep-subwavelength scale in a single-phase metamaterial, Nat. Commun. **5**, 5510 (2014).

[4] K. Yi, M. Collet, M. Ichchou, and L. Li, Flexural waves focusing through shunted piezoelectric patches, Smart Mater. Struct. **25**, 75007 (2016).

[5] X. Su, Z. Lu, and A. N. Norris, Elastic metasurfaces for splitting SV- and P-waves in elastic solids, J. Appl. Phys. **123**, 091701 (2017).

[6] S. Li, J. Xu, and J. Tang, Tunable modulation of refracted Lamb wave front facilitated by adaptive elastic metasurfaces, Appl. Phys. Lett. **112**, 021903 (2018).

[7] L. Cao, Z. Yang, Y. Xu, and B. Assouar, Deflecting flexural wave with high transmission by using pillared elastic metasurface, Smart Mater. Struct. **27**, 075051 (2018).

[8] Y. Xu, L. Cao, P. Peng, X. Zhou, B. Assouar, and Z. Yang, Beam splitting of flexural waves with a coding meta-slab, Appl. Phys. Express **12**, 097002 (2019).

[9] H. Qiu, M. Chen, Q. Huan, and F. Li, Steering and focusing of fundamental shear horizontal guided waves in plates by using multiple-strip metasurfaces, EPL **127**, 46004 (2019).

[10] W. Xu, M. Zhang, J. Ning, W. Wang, and T. Yang, Anomalous refraction control of mode-converted elastic wave using compact notch-structured metasurface, Mater. Res. Express **6**, 065802 (2019).

[11] M. Zheng, C. I. Park, X. Liu, R. Zhu, G. Hu, and Y. Y. Kim, Non-resonant metasurface for broadband elastic wave mode splitting, Appl. Phys. Lett. **116**, 171903 (2020).

[12] J. Rong, W. Ye, S. Zhang, and Y. Liu, Frequency-coded passive multifunctional elastic metasurfaces, Adv. Funct. Mater. **30**, 2005285 (2020).

[13] Y. Liu, H. Li, J. Zhang, X. Liu, L. Wu, H. Ning, and N. Hu, Design of elastic metasurfaces for controlling shear vertical waves using uniaxial scaling transformation method, Int. J. Mech. Sci. **169**, 105335 (2020).

[14] L. Cao, Z. Yang, Y. Xu, S.-W. Fan, Y. Zhu, Z. Chen, B. Vincent, and B. Assouar, Disordered elastic metasurfaces, Phys. Rev. Appl. **13**, 014054 (2020).

[15] P. Mora, M. Chekroun, and V. Tournat, Seismic metashielding by a line of resonators over a granular layer, Phys. Rev. Appl. **16**, 044002 (2021).

[16] W. Wang, J. Iglesias, Y. Jin, B. Djafari-Rouhani, and A. Khelif, Experimental realization of a pillared metasurface for flexural wave focusing, APL Mater. **9**, 051125 (2021).

[17] Y. Jin, W. Wang, A. Khelif, and B. Djafari-Rouhani, Elastic metasurfaces for deep and robust subwavelength focusing and imaging, Phys. Rev. Appl. **15**, 024005 (2021).

[18] Z. Xu, S. Yu, J. Liu, and K. Chuang, A tunable zig-zag reflective elastic metasurface, Crystals **12**, 1170 (2022).

[19] K. Stojanoska and C. Shen, Non-Hermitian planar elastic metasurface for unidirectional focusing of flexural waves, Appl. Phys. Lett. **120**, 241701 (2022).

[20] T. Yang, Z. Lin, X. Zhu, and T. Yang, Elastic metasurface with dual-coupled resonators for highly efficient energy harvesting, Phys. Rev. Appl. **18**, 064065 (2022).

[21] W. Zhou, S. Wang, Q. Wu, X. Xu, X. Huang, G. Huang, Y. Liu, and Z. Fan, An inverse design paradigm of multifunctional elastic metasurface via data-driven machine learning, Mater. Des. **226**, 111560 (2023).

[22] L. Li, K. Su, H. Liu, Q. Yang, L. Li, and M. Xie, Elastic metasurface for flexural wave refraction based on acoustic black hole, J. Appl. Phys. **133**, 105103 (2023).

[23] Y. Jiang, Y. Liu, N. Hu, J. Song, and D. Lau, Continuous-phase-transformation elastic metasurface for flexural wave using notched structure, Int. J. Mech. Sci. **257**, 108563 (2023).

[24] A. Díaz-Rubio and S. A. Tretyakov, Acoustic metasurfaces for scattering-free anomalous reflection and refraction, Phys. Rev. B **96**, 125409 (2017).

[25] A. Epstein and O. Rabinovich, Unveiling the properties of metagratings via a detailed analytical model for synthesis and analysis, Phys. Rev. Appl. **8**, 054037 (2017).

[26] Y. Ra'di, D. L. Sounas, and A. Alù, Metagratings: Beyond the limits of graded metasurfaces for wave front control, Phys. Rev. Lett. **119**, 067404 (2017).

[27] D. Torrent, Acoustic anomalous reflectors based on diffraction grating engineering, Phys. Rev. B **98**, 060101 (2018).

[28] L. Quan, Y. Ra'di, D. L. Sounas, and A. Alù, Maximum Willis coupling in acoustic scatterers, Phys. Rev. Lett. **120**, 254301 (2018).

[29] Z. Hou, X. Fang, Y. Li, and B. Assouar, Highly efficient acoustic metagrating with strongly coupled surface grooves, Phys. Rev. Appl. **12**, 34021 (2019).

[30] Y. Fu, C. Shen, Y. Cao, L. Gao, H. Chen, C. T. Chan, S. A. Cummer, and Y. Xu, Reversal of transmission and reflection based on acoustic metagratings with integer parity design, Nat. Commun. **10**, 2326 (2019).

[31] Y. Wang, Y. Cheng, and X. Liu, Modulation of acoustic waves by a broadband metagrating, Sci. Rep. **9**, 7271 (2019).

[32] Y. Yang, H. Jia, Y. Bi, H. Zhao, and J. Yang, Experimental demonstration of an acoustic asymmetric diffraction grating based on passive parity-time-symmetric medium, Phys. Rev. Appl. **12**, 034040 (2019).

[33] Y. Fu, Y. Cao, and Y. Xu, Multifunctional reflection in acoustic metagratings with simplified design, Appl. Phys. Lett. **114**, 053502 (2019).

[34] Y. K. Chiang, S. Oberst, A. Melnikov, L. Quan, S. Marburg, A. Alù, and D. A. Powell, Reconfigurable acoustic metagrating for high-efficiency anomalous reflection, Phys. Rev. Appl. **13**, 064067 (2020).

[35] Y. Yang, H. Jia, S. Wang, P. Zhang, and J. Yang, Diffraction control in a non-Hermitian acoustic grating, Appl. Phys. Lett. **116**, 213501 (2020).

[36] L. Fan and J. Mei, Metagratings for waterborne sound: Various functionalities enabled by an efficient inverse-design approach, Phys. Rev. Appl. **14**, 044003 (2020).

[37] S. Y. Kim, W. Lee, J. S. Lee, and Y. Y. Kim, Longitudinal wave steering using beam-type elastic metagratings, Mech. Syst. Signal Process. **156**, 107688 (2021).

[38] L. Fan and J. Mei, Multifunctional waterborne acoustic metagratings: From extraordinary transmission to total and abnormal reflection, Phys. Rev. Appl. **16**, 044029 (2021).

[39] L. S. Zeng, Y. X. Shen, X. S. Fang, Y. Li, and X. F. Zhu, Experimental realization of ultrasonic retroreflection tweezing via metagratings, Ultrasonics **117**, 106548 (2021).

[40] Z. Du and J. Mei, Metagrating-based acoustic wavelength division multiplexing enabled by deterministic and probabilistic deep learning models, Phys. Rev. Res. **4**, 033165 (2022).

[41] K. Sun, Y. Fan, S. Chen, F. Yang, J. Li, Q. Fu, and F. Zhang, Highly efficient transmissive wavefront steering with acoustic metagrating composed of Helmholtz-resonators, Mater. Des. **224**, 111352 (2022).

[42] J. Mei, L. Fan, and X. Hong, Elastic metagratings with simultaneous modulation of reflected and transmitted waves, Crystals **12**, 901 (2022).

[43] J. Mei, L. Fan, and X. Hong, Elastic metagratings with simultaneous highly efficient control over longitudinal and transverse waves for multiple functionalities, Phys. Rev. Appl. **18**, 014002 (2022).

[44] X. Li, D. Dong, J. Liu, Y. Liu, and Y. Fu, Perfect retroreflection assisted by evanescent guided modes in acoustic metagratings, Appl. Phys. Lett. **120**, 151701 (2022).

[45] S. Bernard, F. Chikh-Bled, H. Kourchi, F. Chati, and F. Léon, Broadband negative reflection of underwater acoustic waves from a simple metagrating: Modeling and experiment, Phys. Rev. Appl. **17**, 024059 (2022).

[46] Z. Du and J. Mei, Wide-angle and high-efficiency acoustic retroreflectors enabled by many-objective optimization algorithm and deep learning models, Phys. Rev. Mater. **7**, 115201 (2023).

[47] A. Song, C. Sun, Y. Xiang, and F. Z. Xuan, Simple acoustic metagrating for perfect two- and three-beam splitting, Front. Mater. **10** (2023).

[48] X. Zhang, L. Li, K. Li, T. Liu, J. Zhang, and N. Hu, Flexural wave splitting via elastic metagratings based on high-order diffraction theory, Appl. Acoust. **202**, 109170 (2023).

[49] X. Fang, N. Wang, W. Wu, W. Wang, X. Yin, X. Wang, and Y. Li, Extreme wave manipulation via non-Hermitian metagratings on degenerated states, Phys. Rev. Appl. **19**, 054003 (2023).

[50] Y. Ra'di and A. Alù, Nonreciprocal wavefront manipulation in synthetically moving metagratings, Photonics **7**, 28 (2020).

[51] L. Fan and J. Mei, Acoustic metagrating circulators: Nonreciprocal, robust, and tunable manipulation with unitary efficiency, Phys. Rev. Appl. **15**, 064002 (2021).

[52] Y. Jin, X. Fang, Y. Li, and D. Torrent, Engineered diffraction gratings for acoustic cloaking, Phys. Rev. Appl. **11**, 011004 (2019).

[53] J. He, X. Jiang, D. Ta, and W. Wang, Experimental demonstration of underwater ultrasound cloaking based on metagrating, Appl. Phys. Lett. **117**, 091901 (2020).

[54] A. Song, C. Sun, Y. Xiang, and F. Z. Xuan, Switchable acoustic metagrating for three-channel retroreflection and carpet cloaking, Appl. Phys. Express **15**, 024002 (2022).

[55] L. Fan and J. Mei, Achromatic needle focusing with super-resolution enabled by a ring-shaped acoustic metalens, Phys. Rev. Appl. **20**, 054053 (2023).

[56] Y. K. Chiang, L. Quan, Y. Peng, S. Sepehrirahnama, S. Oberst, A. Alù, and D. A. Powell, Scalable metagrating for efficient ultrasonic focusing, Phys. Rev. Appl. **16**, 064014 (2021).

[57] J. Mei, L. Fan, and X. Hong, Broadband and high-numerical-aperture sharp focusing for waterborne sound with metagrating-based lens, New J. Phys. **24**, 093014 (2022).

[58] L. Fan and J. Mei, Flow-permeable and tunable metalens for subdiffraction waterborne-sound focusing, Phys. Rev. Appl. **19**, 024026 (2023).

[59] Y. Bai, A. Song, C. Sun, Y. Xiang, and F. Xuan, Broadband sound focusing with tunable focus based on reconfigurable acoustic coding metagrating, Appl. Phys. Lett. **122**, 261705 (2023).

[60] J. Mei, L. Fan, and X. Hong, Acoustic metalens with switchable and sharp focusing, Appl. Phys. Express **16**, 077002 (2023).

[61] H. Peng, L. Fan, and J. Mei, Simultaneous manipulation of longitudinal and transverse elastic waves with a sharp focusing effect and customizable energy splitting ratios, J. Appl. Phys. **135,** 033102 (2024).

[62] Y. Hu, Y. Zhang, G. Su, M. Zhao, B. Li, Y. Liu, and Z. Li, Realization of ultrathin waveguides by elastic metagratings, Commun. Phys. **5,** 62 (2022).

[63] W. Liu and R. Zheng, Engineered metagrating as shield from surface Rayleigh waves, Mech. Adv. Mater. Struct. (2023).

[64] M. Yang, X. Shen, Z. Li, Z. Wen, G. Chen, Z. Zhang, G. Liang, H. Li, and Z. Shang, High focusing efficiency met-alens with large numerical aperture at terahertz frequency, Opt. Lett. **48,** 4677 (2023).

[65] M. Kang, Y. Ra'di, D. Farfan, and A. Alù, Efficient focusing with large numerical aperture using a hybrid metalens, Phys. Rev. Appl. **13,** 044016 (2020).

[66] G. Chen, Z. Q. Wen, and C. W. Qiu, Superoscillation: From physics to optical applications, Light: Sci. Appl. **8,** 56 (2019).

[67] N. I. Zheludev and G. Yuan, Optical superoscillation technologies beyond the diffraction limit, Nat. Rev. Phys. **4,** 16 (2022).